CFD MODELLING IN THE DEVELOPMENT AND SCALE-UP OF THE HISMELT PROCESS

Mark P. DAVIS[1*] and Rod J. DRY[1]

[1] HIsmelt Corporation, Kwinana, WA 6966, AUSTRALIA

*Corresponding author, E-mail address: mark.davis@riotinto.com

ABSTRACT

The HIsmelt® Process provides an alternative iron making route to the traditional blast furnace. It is a smelt-reduction process involving the injection of iron ore and coal into a molten iron bath and the post-combustion of bath gases by means of an oxy-enriched air jet. At the heart of the process is splash-driven heat transfer between the upper post-combustion zone and the lower bath-smelting zone.

The modelling of droplet and wall heat transfer is crucial to the successful prediction of process performance. A CFD model of the vessel top-space has been developed which uses Lagrangian tracking of iron and slag droplets to simulate the heat and mass transfer processes. Calculation of the slag droplet surface temperature by means of a fully coupled solution of the heat conduction equation inside each droplet is described, and the development of a falling-layer wall model is presented.

NOMENCLATURE

C_p	heat capacity
g	acceleration due to gravity
h	heat transfer coefficient
I	radiation intensity
k	thermal conductivity
$\dot{m}$	mass flow rate
$\dot{q}$	heat flux
r	radius
T	temperature
t	time
u	velocity

Greek Symbols

α	thermal diffusivity
δ	layer thickness
ε	emissivity
Γ_ϕ	exchange coefficient for variable ϕ
μ	dynamic viscosity
ρ	density
σ	Stefan-Boltzmann constant

Subscripts

liq	liquidus	*cnv*	convection
g	gas	*s*	surface
sol	solidus	*w*	wall
lyr	layer		

INTRODUCTION

Direct smelting of iron ore has been investigated over many years as an alternative to the blast furnace. The HIsmelt Process (Goodman, 2007; Bates and Goldsworthy, 2002) provides an alternative ironmaking route which arguably meets the challenge of increasing environmental and cost pressures that face the global steel industry. This process, developed by Rio Tinto over a period of 25 years, advanced to an 800,000 t/a commercial plant jointly owned by Rio Tinto, Nucor Corporation, Mitsubishi Corporation and Shougang Corporation. This plant built in Kwinana, Western Australia, was hot commissioned in April 2005 and operated for 3 years until December 2008.

The process offers potential environmental and cost advantages over the blast furnace such as the elimination of coke ovens and sinter plants which have significant greenhouse gas and other emissions as well as waste disposal issues. It uses fine iron ores and non-coking coal directly by injecting them into a molten bath at high velocity, and has demonstrated operational flexibility in using a wide range of ferrous feeds and coal types. An added advantage is that phosphorus reports to the slag, so it suits the processing of high phosphorus ores which are abundant in Western Australia.

Development of the process has progressed through a number of pilot plant scales and designs each of which has been aided by the use of physical and computational fluid dynamics (CFD) models. Scale up of any metallurgical process is never straight forward due to the increasing scales over which turbulent flow processes operate. Understanding the fluid dynamics involved and the associated heat and mass transfer processes has therefore been a key aspect of understanding the behaviour of the process and enabling the progression to larger smelting vessels with a higher degree of confidence than would otherwise be possible.

HIsmelt initiated CFD modelling work in the early 1980's with CHAM Ltd and the CSIRO, each group investigating different aspects of the process using the PHOENICS CFD code. Over the intervening years modelling work has also been carried out using the PHYSICA and FLUENT codes and has more recently been transferred to the ANSYS-CFX platform where all the current work is being performed.

Process Description

At the core of HIsmelt is the Smelt Reduction Vessel (SRV) which is illustrated in Figure 1. It consists of a water-cooled upper shell and a refractory hearth. The process uses high-velocity injection of coal and ore into the melt via downwardly-angled water-cooled injection lances. Injected coal, after heating and devolatilisation, dissolves to maintain around 4% carbon in metal. Injected ore is then brought into contact with this carbon-rich metal, and smelting occurs as represented by:

$$3[C]_{iron} + Fe_2O_3 \rightarrow 2[Fe]_{iron} + 3CO \quad (1)$$
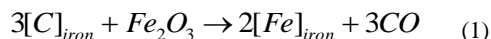
The lower part of the SRV is maintained at a low oxygen potential to allow this endothermic reaction to occur.

Heat supply to maintain the necessary thermal balance comes from post combustion of bath gas (mainly CO) in the upper part of the vessel. Oxygen-enriched hot blast (typically 35% total oxygen at 1200 °C) is introduced via a top lance, and combustion occurs in the relatively oxidizing region of this upper section. Swirl is added to the blast, via vanes located within the lance, to increase the rate of combustion as represented by:

$$2CO + O_2 \rightarrow 2CO_2 \quad (2)$$

$$2H_2 + O_2 \rightarrow 2H_2O \quad (3)$$
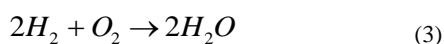
At the heart of the process is the splash-driven heat transfer between the hot post combustion gases in the upper part of the vessel and the smelting zone below. Splash is generated from the large volume of gas that is generated within the bath from the ore reduction and coal devolatilisation processes. The rate of bath gas generation is equivalent to replacing the bath volume every 1.6 seconds. Not surprisingly this large production of gas results in a violent eruption of liquid metal and slag from the bath surface which in turn produces a gas permeable fountain with high surface area for heat transfer.

The heat generated by post combustion of the bath gases will either transfer to the bath (via the fountain of slag and metal droplets), to the water-cooled panels (which line the upper parts of the vessel) or will heat up the process offgas. Evidently, high heat-transfer efficiency to the bath is the desired outcome to maximise the metal production rate of the vessel.

HIsmelt Flow Models

A significant amount of CFD and physical modelling has been used by HIsmelt to assist in the development and scale up of the process. The SRV has been modelled using two linked CFD models: the "bath model" (Stephens et al, 2011) and the "topspace model" (Davis et al, 2003).

The bath model covers the volume of the vessel occupied by the bath and the fountain of droplets but does not model the hot blast. It is an isothermal model which attempts to simulate the bath dynamics. It is a three dimensional transient multiphase multi-component Eulerian-Eulerian reactive CFD model that incorporates both Lagrangian tracking of ore/coal particles and an algebraic slip model to allow for both slag and metal components in the liquid bath.
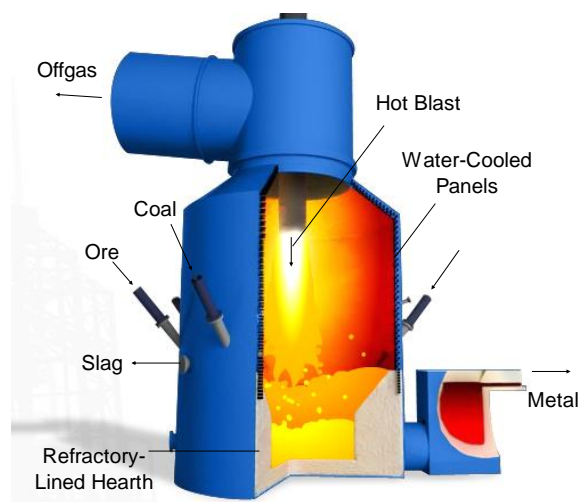
Figure 1: The HIsmelt Smelt Reduction Vessel.

The topspace model covers the volume above the slag surface occupied by the fountain and the hot blast. It simulates the flow of gas and liquid droplets from the bath surface and the combustion of this gas by the hot blast. Account is also taken of the flow and combustion of char and soot particles from the bath, heat transfer to the vessel walls, and radiation. The model includes the effects of droplet breakup, droplet decarburisation by process gases, and droplet heat transfer.

Modelling of the physical processes occurring within the bath represents a substantial CFD challenge. The small timescales involved mean that a time-step of the order 0.8 ms is required to achieve convergence with 10 iterations per time step. It can therefore take a number of days to simulate just 10 seconds of real-time using parallel computing on a high-end desktop computer. This barely gets past the transients associated with starting from time zero when there is just the quiescent bath and no injection of feed materials. It is for this reason that the SRV volume has been simulated using two quite different CFD models. There is of course overlap between the two models and the flow of gas and liquid from the bath surface predicted by the bath model can serve as inflow boundary conditions for the topspace model. The topspace model is a steady-state model which uses Lagrangian tracking of the liquid metal and slag droplets. It can therefore be used for design and scale-up analyses, as it takes comparatively much less time to run than the bath model.

Detailed descriptions of the bath and topspace models are given elsewhere (Stephens et al, 2011 and Davis et al, 2003 respectively). In this work the focus has been on the development of an efficient calculation of the slag droplet surface temperature and the development of a falling-layer wall model.

SLAG DROPLET SURFACE TEMPERATURE

Standard Lagrangian models of heat transfer to particles or droplets use an energy balance over the particle to derive the bulk temperature variation with time. This balance takes account of heat and mass transfer as well as radiative heat transfer. In the current context the large thermal mass of the iron and slag droplets (which are typically

2

characterised as being 1 mm to 30 mm in diameter) results in a droplet temperature rise of only a few tens of degrees. However it is recognised that slag droplets, with a thermal conductively of roughly 1 W/m.K, will develop a large radial temperature gradient during their short (~1 second) journey through the topspace, the droplet surface being considerably hotter than the bulk. High slag viscosity will also limit the internal rate of heat transfer arising from drag-induced recirculation of the droplets. These effects will have a significant impact on the amount of heat transfer between the topspace gas and the slag. Calculation of the slag droplet surface temperature by means of a fully coupled solution of the heat conduction equation has therefore been developed and implemented within the CFX framework as described below.

The transient heat conduction equation within a spherical droplet can be written:

$$\rho \, C_p \, \frac{\partial T}{\partial t} \;=\; \frac{1}{r^2} \frac{\partial}{\partial r}\left(k \, r^2 \, \frac{\partial T}{\partial r} \right) \qquad (4)$$

where ρ and Cp are the droplet density and specific heat capacity respectively, r is the distance from the centre of the droplet and k is the thermal conductivity.

The boundary conditions for the droplet temperature are given by:

$$\left. \frac{\partial T}{\partial r} \right|_{r=0} \;=\; 0.0, \text{ and}$$

$$k \left. \frac{\partial T}{\partial r} \right|_{r=R} = h_{cnv}\left(T_g - T_s \right) + \varepsilon \left(\pi I - \sigma T_s^4 \right) \qquad (5)$$

where h_{cnv} is the gas convective heat transfer coefficient (calculated using standard empirical relations based on the Nusselt number), the subscripts g and s refer to the gas and droplet surface respectively, ε is the slag surface emissivity, and I is the radiation intensity.

A uniform temperature profile within the droplet at time zero is assumed and is set equal to the slag layer temperature.

One approach to solving Eq. (4) is to assume a parabolic temperature profile for the droplet. Integration then leads to T_s as a function of the heat transfer conditions at the surface and the droplet properties (e.g., Dombrovsky and Sazhin, 2003). Whilst this might be appropriate for small droplets undergoing continuous heating, varying conditions through the topspace may result in cooling as well as heating of the droplet. There is not therefore a general profile that will fit all conditions which a droplet may experience. The numerical solution of heat conduction within a slag droplet has therefore been implemented using the finite difference form of Eq. (4). This can be written:

$$\frac{T_P - T_P^o}{\delta t} \;=\; \frac{\alpha}{r_P^2 \, \delta r_P} \left[\left. \Gamma_n \frac{\partial T}{\partial r} \right|_n - \left. \Gamma_s \frac{\partial T}{\partial r} \right|_s \right] \qquad (6)$$

where $\Gamma_i = r_i^2$, the subscripts n, s denote values on the faces of the control volume north and south of the integration point P, and the superscript o refers to the old time step value. Making suitable approximations for the radial temperature gradients Eq. (6) can be rearranged to

give the droplet temperature at point P (in standard CFD notation):

$$T_P \;=\; \frac{A_n \, T_N + A_s \, T_S + S_c}{A_n + A_s + S_p} \qquad (7)$$

The standard tri-diagonal matrix algorithm (TDMA), a simplified form of Gaussian elimination, can be used to solve Eq. (7) yielding:

$$T_i \;=\; P_i \, T_{i+1} \;+\; Q_i \qquad (8)$$

where

$$P_i = \frac{A_n}{A_p + S_p - A_s \, P_{i-1}} \,, \quad Q_i = \frac{S_c + A_s \, Q_{i-1}}{A_p + S_p - A_s \, P_{i-1}}$$

To complete the solution the boundary conditions specified by Eq. (5) need to be incorporated. This is achieved by using the approximation:

$$\left. \frac{\partial T}{\partial r} \right|_{r=R} \;=\; \frac{T_s - T_P}{0.5 \, \delta r_p} \qquad (9)$$

in Eq. (5) to yield:

$$\varepsilon \, \sigma \, T_s^4 + \left(h_{cnv} + \frac{k}{0.5 \, \delta r_P} \right) T_s -$$
$$\left(h_{cnv} T_g + \varepsilon \pi \, I + \frac{k}{0.5 \, \delta r_P} T_P \right) = 0 \qquad (10)$$

The temperature T_p in this equation (ie. the temperature at the finite-difference node next to the droplet boundary) can be derived in terms of the surface temperature, T_s, by considering the TDMA solution at the boundary cell, viz:

$$T_{p=N} = Q_N = \frac{S_c + A_s \, Q_{N-1}}{A_s + S_p - A_s \, P_{N-1}} \qquad (11)$$

The source terms in Eq. (11) contain the temperature gradient at the droplet surface, viz:

$$\left. \Gamma_n \frac{\partial T}{\partial r} \right|_n \;=\; \Gamma_n \frac{T_s - T_P}{0.5 \, \delta r_P} \qquad (12)$$

and hence Eq. (11) can be written in the following form:

$$T_{p=N} \;=\; \frac{C_1 + C_2 \, T_s}{C_3} \qquad (13)$$

Substitution of Eq. (13) into Eq. (10) yields the final form of the equation for the droplet surface temperature:

$$\varepsilon \, \sigma \, T_s^4 + \left(h_{cnv} + \frac{k}{0.5 \, \delta r_P} \left(1 - \frac{C_2}{C_3} \right) \right) T_s -$$
$$\left(h_{cnv} T_g + \varepsilon \pi \, I + \frac{k}{0.5 \, \delta r_P} \frac{C_1}{C_3} \right) = 0 \qquad (14)$$

Equation (14) can be solved using Newton-Raphson, and the droplet surface temperature, T_s, used to calculate the boundary droplet temperature (Eq. (13)). The droplet temperature profile is then completed using the TDMA procedure of Eq. (8). Given the small time steps used by the Lagrangian particle-tracking procedure, the NR calculation generally converges within a couple of iterations and is not therefore computationally expensive.

The implementation of this calculation within ANSYS CFX version 14 is achieved using the particle additional variable (PAV) model. This has been implemented to be broadly analogous to fluid algebraic additional variables in CFX and is used to represent the instantaneous droplet temperature at a user-defined number of radial shells

within the droplets. Generally the surface temperature and 20 internal temperatures are solved. The finite-difference grid used for this calculation is dependent on the droplet diameter and is calculated and stored (along with the TDMA coefficients) at the start of each track. A power-law grid distribution has been used which concentrates the grid close to the droplet radius for large droplets (eg. a power of 0.3 is used for 3 cm droplets) and modifies to a uniform grid for any droplet less than 1mm in diameter.

Verification of this calculation has been made by comparison with a CFX model of a conducting sphere (Staples et al, 2010). This showed some minor discrepancies near to the sphere's centre that were attributed to the use of a vertex based scheme in CFX compared to the element based scheme employed here, and to CFX solving the conduction equation in Cartesian coordinates compared to spherical coordinates. Given the droplet centre, in most cases, will remain at the initial temperature in the topspace simulations, this discrepancy is not considered significant.
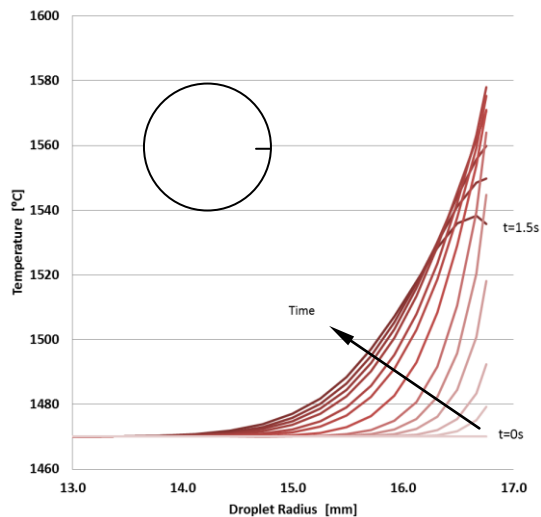
Figure 2: Temperature profiles for a 33mm droplet (insert illustrates the droplet radius over which this figure is plotted).

Figure 2 shows a typical transient temperature profile for a 33mm droplet travelling through the topspace. In this instance the droplet takes 1.5 seconds to rise from and then return to the bath surface. In this time the surface temperature increases by 90 degrees before losing over 40 degrees as the droplet descends to the bath in a relatively cooler local environment.

The variation in gas temperature through the HIsmelt topspace is reflected in the droplet surface temperature tracks of Figure 3. The combustion zone beneath the HAB lance is clearly evident as is the relatively cooler gases leaving the vessel through the off-take.
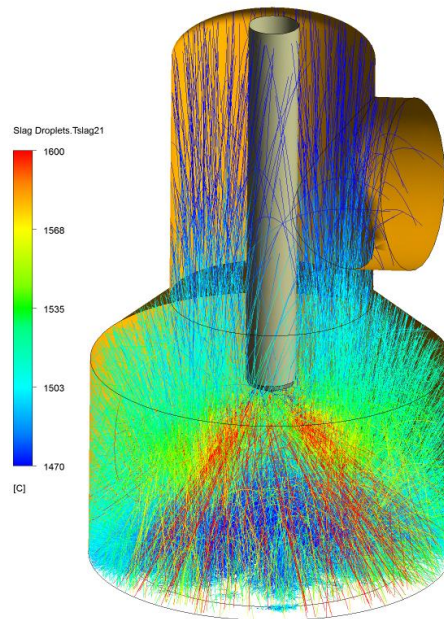
Figure 3: Slag droplet tracks within the topspace coloured by droplet surface temperature.

WALL MODEL

Specification of the wall thermal boundary conditions in the top space of the vessel requires characterisation of the thermal environment to which the walls are subjected. In particular, the intermittent splashing of the walls means steady-state wall conditions are required for a process which is intrinsically dynamic in nature. Dependent on height within the vessel (and the size of the droplet fountain), splash can wash the walls with a timescale ranging from a few seconds to a few minutes or even longer.

The vessel walls consist of water cooled panels initially encased within a castable refractory which is replaced as the process is 'fired up' with an attached layer of frozen slag. This frozen layer will build up over time until its surface reaches a temperature at which it no longer completely freezes but rather forms a mix of liquid and partly crystallised slag components. At this point additional splash will form a mushy layer on the wall and flow downwards under the influence of gravity. In addition high melting point components of the slag will continue to grow from the frozen slag layer forming dendritic type structures. The temperature at which this happens will be between the slag solidus and liquidus temperatures (a range of roughly 140 degrees for a typical HIsmelt slag).

Modelling of slag layers for entrained flow gasifiers has been developed on the basis of negligible inertial forces and pressure gradient for the equation of motion, and on the assumption that convection and viscous dissipation are insignificant in the heat flow equation (Bockelie et al, 2003). The latter assumption implies that conduction is the principle heat transfer mechanism across the slag layer. Heat convection is only considered in a heat balance over an element which covers the width of the layer. Previous topspace model work has used the standard equations for laminar flow of a falling film to model this layer, but it

4

was recognised that this ignores the formation of a mushy zone of slag adjacent to the frozen slag.

Falling Layer Model

To further investigate the flow and heat transfer behaviour of the slag layer flowing down the vessel walls a two-dimensional model has been constructed as shown in Figure 4. The domain is 5m high and the width is set according to the falling layer width being simulated (usually in the range 2 to 8mm). A grid of 50 cells across the layer and 1000 cells down the layer was generally used.
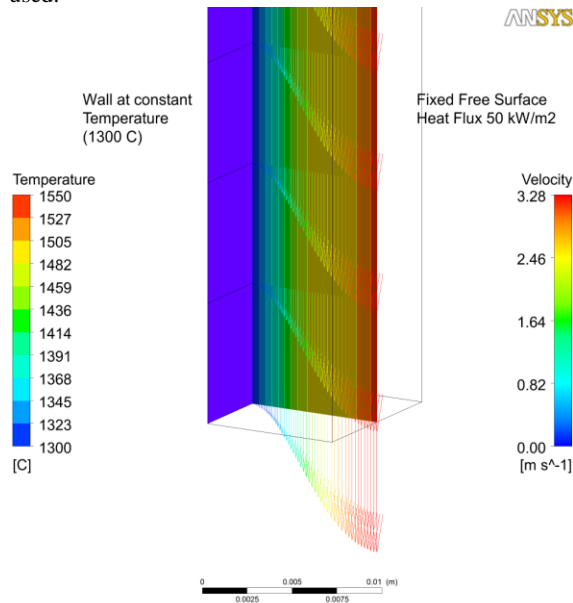
Figure 4: Velocity vectors and gas temperature contours for an 8mm slag layer (bottom of domain 5m from inflow)

A realistic model of a 'naturally' falling layer would consist of a fixed mass flow rate of slag and a layer width determined by the development of the flow as it travels down the wall. However, this free-surface approach has significant modelling challenges and therefore a simple fixed-width approach has been used. The layer mass flow has been set according to the equations for a fully developed layer (Equation 20 below). For the HIsmelt slag this is not true for the thermal boundary layer and given the layer viscosity is a strong function of temperature the shear stress across the layer will vary as the slag travels down the wall. This can lead to the layer velocity profile being slightly out of balance with the layer shear stress but the effect on the velocity profile is small and for the present purposes this approach is considered adequate.

Another difficulty with this model is how to define the temperature at which the frozen slag layer is behaving as a "wall". The temperature at which there is very little downward movement of the falling layer will depend on the viscosity-temperature relationship of the slag in question and on the strength of the dendritic structures that grow out from the wall. In addition, the width of the falling layer will have an impact as a larger layer will impose greater shear on the material next to the frozen slag. In the present model the "wall" temperature has been defined as the slag temperature at which there are 50% solids. This is quite arbitrary and the sensitivity of model results to this assumption will need to be tested.

Nonetheless the wall is modelled as a "no-slip" boundary condition.

The HIsmelt slag exhibits a rapid increase in viscosity as the temperature drops below the liquidus temperature. FactSage calculations (Grundy et al, 2008) have been used to predict the formation of solid phases and their impact on the slag viscosity for a slag comprising 36% CaO, 29% SiO_2, 14% Al_2O_3, 9% MgO and 8% FeO as shown in Figure 5. For temperature values above the liquidus temperature, the FactSage data has been approximated using the following relationship:

$$\mu' \; = \; 0.2909 \; e^{-0.0054\left(T - T_{liq}\right)} \qquad (15)$$

where T_{liq} is the slag liquidus temperature. Between the liquidus and solidus temperatures the viscosity is expressed as a function of the solids fraction to give the final form of the viscosity relationship as:

$$\mu \; = \; \mu' \; e^{\left(2.7 \, f_s\right)} \qquad (16)$$

where

$$f_s \; = \; \begin{cases} 0 & T > T_{liq} \\ 1 & T < T_{sol} \end{cases}$$

otherwise

$$f_s \; = \; \begin{cases} \dfrac{T_{Liq} - T}{T_{Liq} - T_{sol}} \end{cases}$$
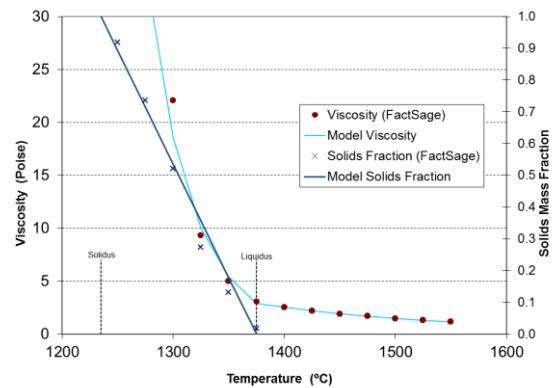
Figure 5: Viscosity of the HIsmelt slag.

The surface of the falling layer is modelled as a wall with zero shear stress (free-slip condition) and has a fixed heat flux applied to account for heat flow from the topspace gas.

Data for slag thermal conductivity of a typical HIsmelt slag is not easily found in the literature, and is further complicated by the presence of entrained metal prills and gas bubbles. Due to the high level of crystallisation at low temperatures and lower degree of polymerisation at higher temperatures, slag conductivity varies significantly with temperature. The relatively high conductivity of metal also has a large impact although this is negated somewhat by the low conductivity of gas bubbles. Even with all this uncertainty the inclusion of the temperature functionality of the slag conductivity was considered an improvement over simply assuming a constant value. The data of Susa (Susa et al, 1993) for a slag composition of 49.5% CaO, 10% Fe_2O_3 and 40.5% SiO_2 has been used with estimates of 10 % metal (by mass) and 10% gas (by volume) to produce the following thermal conductivity relationship:

$$k = \frac{485}{T-900} \qquad (17)$$

For the simulations presented here the slag layer density and heat capacity have been taken as 2300 kg/m^3 and 1200 J/kg K respectively. The Prandtl number of the HIsmelt slag, it should be noted is therefore high throughout the layer (ie it ranges from ~1500 to 200) indicating that heat diffusion through the falling slag layer will be slow compared to momentum diffusion.

As mentioned above, the work on entrained flow gasifiers has detailed a method for determining the velocity profile on the assumption of thermal equilibrium across the layer. Using the same approach but with the thermal conductivity relationship of Equation (17) the velocity profile across the layer is given by:

$$u(T_{lyr}) = \frac{485\rho\, g}{\dot{q}^2} \int_{T_{wall}}^{T_{lyr}} \frac{k(T)}{\mu(T)} \ln\left(\frac{T_s - 900}{T - 900}\right) dT \qquad (18)$$

where $\dot{q}$ is the heat flux being conducted across the layer, obtained by integration of Fourier's law as:

$$\dot{q} = \frac{1}{\delta}\int_{T_{wall}}^{T_s} k(T)\, dT = \frac{1}{\delta} 485 \ln\left(\frac{T_s - 900}{T_{wall} - 900}\right) \qquad (19)$$

Equation (18) together with mass conservation across the layer yields the layer mass flow rate as:

$$\dot{m} = \frac{\rho}{\dot{q}} \int_{T_{wall}}^{T_s} k(T)\, u(T)\, dT \qquad (20)$$

For a given heat flux and layer width the surface temperature is given by Equation (19) and then Equations (18) and (20) can be numerically integrated using Simpson's rule to yield the layer velocity profile and mass flow rate.

Wall Model Results

Radial temperature and velocity profiles for 8mm and 4mm slag layers are shown in Figures 6 and 7 respectively. Profiles are shown at 1m intervals down the wall together with the equilibrium solutions given by Equations (18) to (20). The initial temperature of the slag was 1500 $^{\circ}$C, and in both cases the surface heat flux was 50 kW/m^2.

It is apparent that even after 5m of travel the slag layer has not reached thermal equilibrium. For the 8mm layer the thermal boundary layer next to the wall has only penetrated halfway across the layer, whilst the surface boundary layer extends only 1mm from the surface.
Thermal equilibrium is almost achieved for the 4mm layer, but it should be remembered that the layer profiles are highly dependent on the initial temperature of the slag, whilst the equilibrium profiles are only dependent on the surface heat flux. So if the initial slag temperature had been higher, at say 1600 $^{\circ}$C, a much greater difference would be evident between the layer and equilibrium profiles.

In contrast, the velocity profiles are developed within a short distance (Figure 7) as a result of the high viscosity of the slag layer. However given enough distance the 8mm layer will reach equilibrium, so the velocity profiles will keep on changing down the wall as the temperature profile develops and impacts on the slag viscosity.

The 'entry' effect of the thermal boundary layer is clearly evident in figures 8 and 9 which show the heat flux to the frozen slag layer (ie the wall) as a function of the distance down the layer. There is an extremely high heat flux at the start of the layer, where there is effectively a step change in temperature between the wall and the layer, which then rapidly decreases as the boundary layer develops. Figure 8 shows the effect of the initial slag temperature on the wall flux for an 8mm layer. As would be expected increasing the layer temperature increases the wall flux. The impact of the surface heat flux (ie the heat flux from the topspace) on the wall heat flux is shown in Figure 9 for a 4mm layer. Here the entry effect is identical and it is not until 1m downstream when the two thermal boundary layers start to merge that the increase in the surface flux is evident in the heat flux to the wall. However, the 100 kW/m^2 surface heat flux still only results in a 78 kW/m^2 heat flux to the wall so this 4mm layer is still a long way from thermal equilibrium.

Wall Model Discussion

These preliminary investigations into the nature of the falling slag layer on the HIsmelt vessel walls have highlighted the sensitivity of the wall heat flux to the thermal conditions of the slag. It is evident that increasing the splash to the walls and therefore the resulting layer thickness will have a marked effect on the net heat transfer to the water-cooled panels.

From a CFD modelling perspective, the aim of these investigations was to assess if a simple formulation of the layer equations, along the lines employed for entrained flow gasifiers could be developed with the aim of developing a means for more accurately setting the wall temperature boundary condition in the topspace model and also predicting the resultant wall heat flux. However, it is apparent that the 'gasifier equations' will not yield accurate predictions beyond their equilibrium assumptions, and, for the HIsmelt slag, this implies applicability is limited to layers less than approximately 4mm in width. Further work in this area is ongoing.

CONCLUSION

Understanding the heat transfer mechanisms within the topspace of the HIsmelt vessel is crucial for understanding plant performance and the development and scale-up of the process. Further developments in the modelling of topspace heat transfer have been presented. The calculation of slag surface temperature by the efficient solution of the fully coupled heat conduction equation inside each droplet has been implemented and is a significant improvement on the bulk temperature approach. Models of the falling slag layer on the vessel walls reveal the impact of slag thermal characteristics on the insulating effect of this layer. Ongoing development of the wall model is required to account for the non-equilibrium nature of the slag layer.
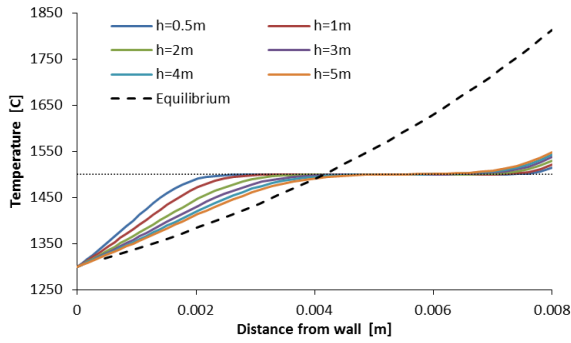
Figure 6(a): Radial Temperature profiles across an 8mm layer (at heights from the inlet).
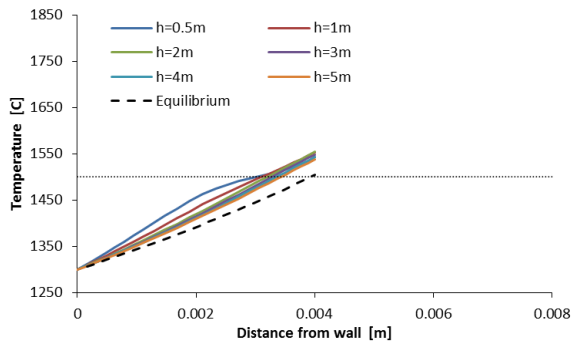
Figure 6(b): Radial Temperature profiles across a 4mm layer.
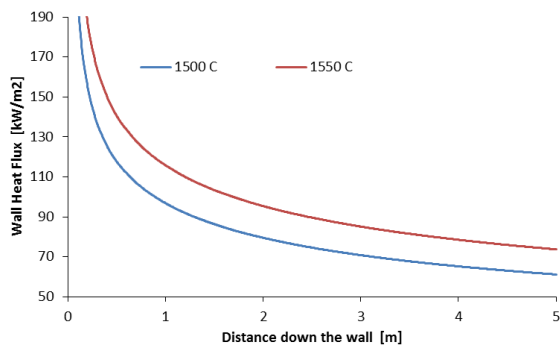
Figure 8: Effect of initial slag temperature on wall heat flux for an 8mm layer (50 kW/m^2 surface flux).
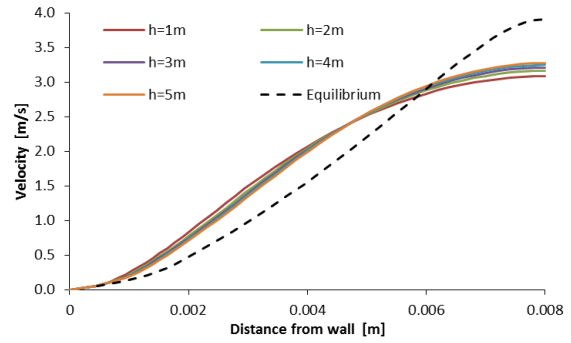
Figure 7(a): Radial Velocity profile across an 8mm layer.
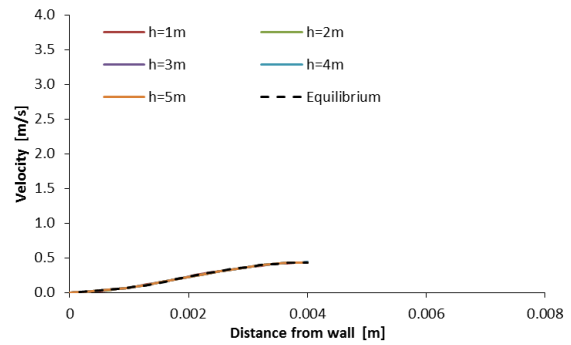
Figure 7(b): Radial Velocity profile across a 4mm layer.
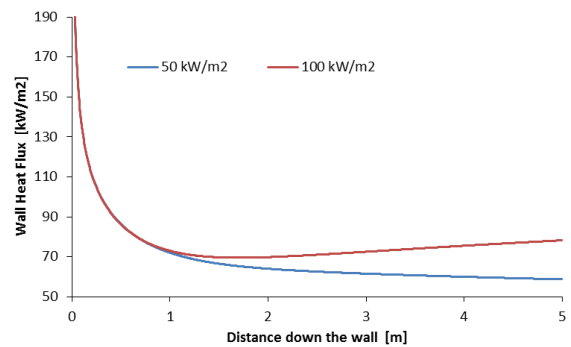
Figure 9: Effect of surface heat flux on wall heat flux for a 4mm layer (1500℃ initial slag temperature).

REFERENCES

BATES, P. and GOLDSWORTHY, T., (2002), "HIsmelt – Meeting the Global Steel Industry Challenge", *1st Japan-Australia Symp. on Iron & Steelmaking,* Fuwa-Ward Symposium, Kyoto.

BOCKELIE, M.J., DENISON, M.K., CHEN, Z., LINJEWILE, T., SENIOR, C. L., and SAROFIM, A.F.; (2002), "CFD modelling of Entrained Flow Gasifiers for Vision 21 Energyplex Systems", *Proc. of the 19th Int. Pittsburgh Coal Conf.*, Pittsburg, PA, USA, 24-26 Sept.

DAVIS, M., DRY, R., and SCHWARZ, M.P., (2003), "Flow Simulation of the HIsmelt Process", *3rd Int. Conference on CFD in the Mineral and Process Industries,* CSIRO, Melbourne, Australia, 10-12 Dec.

GRUNDY, A.N., LIU, H., JUNG, I.H., DECTEROV, S.A., and PELTON, A.D., (2008), "A model to calculate the viscosity of silicate melts", *Int. J. Materials Research*, **99**, 1185-1209.

DOMBROVSKY, L.A., and SAZHIN, S.S., (2003), "A Parabolic Temperature Profile Model for Heating of Droplets", *J. of Heat Transfer*, **125**, 535-537.

GOODMAN, N., (2007), "Operations at the HIsmelt Kwinana Plant", *AIST Conference Indianapolis,* Indiana.

STEPHENS, D., TABIB, M., DAVIS, M., and SCHWARZ, M.P., (2011), "CFD Simulation of Bath Dynamics in the HIsmelt Smelt Reduction Vessel for Iron Production", *8th Int. Conference on CFD in Oil & Gas, Metallurgical and Process Industries,* SINTEF/NTNU, Trondheim, Norway, 21-23 June.

STAPLES, C., and HAMILL, I., (2010), "Inclusion of Particle Additional Variables in ANSYS CFX", *ANSYS project report number 32-10-1-W69R1*, October.

SUSA, M., LI, F., and NAGATA, K., (1993), "Thermal conductivity, thermal diffusivity, and specific heat of slags containing iron oxides", *Ironmaking and Steelmaking*, **20**(3), 201-206.